



Atomically dispersed manganese-based catalysts for efficient catalysis of oxygen reduction reaction

Lu Bai^{a,1}, Zhiyao Duan^{b,1}, Xudong Wen^a, Rui Si^c, Jingqi Guan^{a,*}

^a Key Laboratory of Surface and Interface Chemistry of Jilin Province, College of Chemistry, Jilin University, Changchun, 130021, PR China

^b Department of Chemistry and Institute for Computational and Engineering Sciences, The University of Texas at Austin, Austin, Texas, 78712-1224, USA

^c Shanghai Institute of Applied Physics, Chinese Academy Sciences, Shanghai, 201204, China

ARTICLE INFO

Keywords:

Density functional theory

MnN₄

Nitrogen-doped graphene

Oxygen reduction reaction

Single atom catalysis

ABSTRACT

Rational design and preparation of earth-abundant materials with high-efficiency oxygen reduction reaction (ORR) performance is pivotal for fuel cells. Here, an atomically dispersed Mn- and nitrogen-codoped graphene material (Mn@NG) is developed by a facile high-temperature annealing and subsequent acid-leaching strategy. The atomically dispersion of manganese in Mn@NG is confirmed by aberration-corrected electron microscopy with atomic resolution and the main structure of MnN₄ moiety is resolved by X-ray absorption spectroscopy. The Mn@NG catalyst shows an onset potential and half-wave potential of 0.95 and 0.82 V vs RHE in 0.1 M KOH solution, respectively. Theoretical calculations manifest that MnN₄ moiety embedded into graphene is the active center for efficient ORR, on which the theoretical overpotential is 0.63 V, lower than that on graphitic-N (1.18 V), pyridinic-N (1.58 V), MnN₃-G (1.48 V), MnN₃O-G (2.33 V), and Mn₃O₄ (001) surface (0.86 V).

1. Introduction

Oxygen reduction reaction (ORR) with sluggish kinetics severely limits energy efficiency of proton-exchange membrane fuel cells (PEMFCs). [1–4] Although platinum-based catalysts can catalyze the ORR with low overpotential, the low abundance and high price severely impede a wide range of application in fuel cells. [5,6] Therefore, development of cost-efficient and high-efficiency Pt-free ORR electrocatalysts is pivotal to practical application in fuel cells. [7–9] For the pure carbon materials, a two-electron pathway is predominant during electrocatalytic ORR, which takes place on the carbon atoms adjacent to oxygen functional groups and hydrogen peroxide (H₂O₂) is the main product. [10] For nitrogen-doped carbon materials, the ORR activity is lower than that on metal and nitrogen co-doped materials and both four-electron pathway and 2 + 2 electron pathway were proposed [11,12]. For MN₄-based complexes, Cr corroles, Mn corroles, and Co corroles can catalyze ORR with dominant two-electron pathway to yield H₂O₂ due to the high energy barrier for heterolytic O–O bond cleavage of peroxo intermediates, [13–15] while Fe porphyrins and Cu corroles can catalyze the 4e[−] reduction of oxygen to water [16–18]. However, the electron transfer rate of Co corroles can be accelerated by covalently anchoring them on carbon nanotubes, which can efficiently enhance the 4e[−] ORR activity.[19] It is an effective approach to

synthesize ORR catalysts by immobilizing molecular catalysts onto a support with good electrical conductivity.

It is well-known that Fe/Co- and N- codoped carbon materials shows very high ORR activity and are the most promising ORR catalysts to substitute precious metal Pt. [3,20] The main active sites should be MN₄C_x moiety, on which the reaction can take place with lower energy barrier than on other sites, such as MN₃C_x and MN₂C_x moieties. [21,22] However, although much research has been done to develop various Fe/Co- and N- codoped carbon materials, the Fe or Co ions would be slowly dissolved due to the participation in Fenton reactions, which leads to the deactivation. [23] Comparatively speaking, the reactivity between Mn and H₂O₂ is weaker than that between Fe/Co and H₂O₂, which favors the stability and thus the Mn-based catalysts show potential application in fuel cells. [23,24]

For manganese-based electrocatalysts, the ORR performance can be greatly ameliorated by increasing the surface area and adjusting the average valence of Mn between Mn^{III} and Mn^{IV} [25–27]. In addition, regulating the electronic structure of Mn by appropriate ligands is another efficient method to enhance the catalytic activity. For instance, the ORR activity of Mn porphyrins can be enhanced by embellishing the porphyrin ligands with electron-donating groups to augment the electron concentration around the central Mn ion. [18] Manganese and nitrogen codoped graphene with MnN₄C_x active site is theoretically

* Corresponding author.

E-mail address: guanjq@jlu.edu.cn (J. Guan).

¹ These authors contributed equally to this work.

predicted to possess comparable ORR activity with the Pt catalyst. [28] However, although it has been calculated from the first-principles molecular dynamics simulation that the MnN_4C_x active site is stable at high annealing temperature, synthesis of heterogeneous Mn-based catalysts with pure MnN_4C_x structure is very challenging because Mn ions are easily aggregated during the high-temperature treatment even at a low content. [23] Wu et al reported a carbonization of Mn-doped ZIF-8 precursors to obtain atomically dispersed MnN_4 moieties embedded carbon framework, which shows excellent ORR performance in acidic media. [23]

Here we report atomically dispersed manganese embedded into nitrogen-doped graphene (Mn@NG) by facile annealing and acid-leaching strategy for efficient catalysis of ORR. X-ray absorption spectroscopy characterization and density functional theory (DFT) calculations reveal that mononuclear manganese site coordinated with four nitrogen atoms in the graphene framework should be the active site for ORR.

2. Results and discussion

The Mn@NG and Mn@G catalysts can be conveniently synthesized by annealing the Mn^{2+} /graphene oxide precursor under flowing

ammonia or argon atmosphere and by subsequent acid treatment. The typical morphology of Mn@NG and Mn@G is depicted in Fig. 1 and Fig. S1. No MnO_x nanoparticles but only atomically dispersed manganese can be observed in Mn@NG by the aberration-corrected high angular annular dark-field scanning transmission electron microscopy (STEM). Additionally, no detectable peaks can be attributed to the MnO_x nanoparticles from the Raman spectra (Fig. S2). Element mapping using energy dispersive X-ray spectroscopy (EDS) coupled with STEM was performed to analyze the compositional distributions of Mn@NG , which show that C, O, N and Mn are uniformly distributed throughout the selected region (Figs. 1c and 1d). The Brunauer–Emmett–Teller (BET) surface area of Mn@G and Mn@NG are found to be 347, and $376 \text{ m}^2 \text{ g}^{-1}$, respectively.

XPS spectrum indicates the existence of carbon, nitrogen, oxygen, and manganese elements for Mn@NG (Fig. 2a), but no N for Mn@G (Fig. 2a). The surface element content of Mn@G and Mn@NG is listed in Table S1, which shows 7.9% of N and 0.032% of Mn on the surface of Mn@NG . The C 1s XPS spectrum of Mn@NG can be decomposed into three peaks due to C=C, C–N, and C–O (Fig. S3). [29,30] The N 1s XPS spectrum of Mn@NG can be deconvoluted into five peaks, associated with pyridiniC–N, Mn–N_x, pyrroliC–N, graphitiC–N, and oxidized-N (Fig. 2b). [23,31] The high-resolution Mn2p spectra of Mn@G and

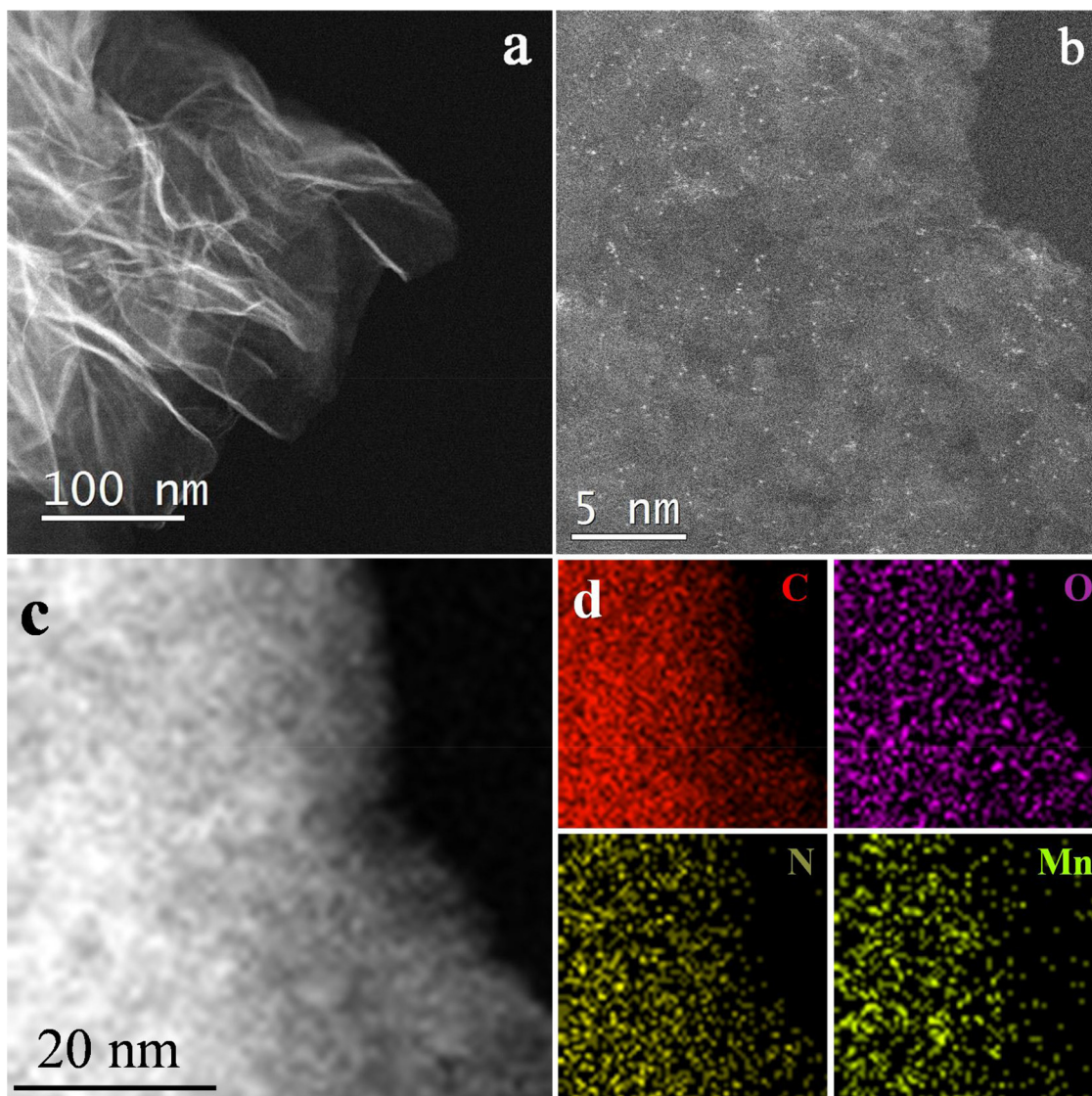


Fig. 1. (a, b) HAADF-STEM images of Mn@NG with different magnifications, (c) HAADF-STEM image of Mn@NG used in the EDS elemental mapping test, and (d) the corresponding EDS elemental mapping of C, O, N and Mn.

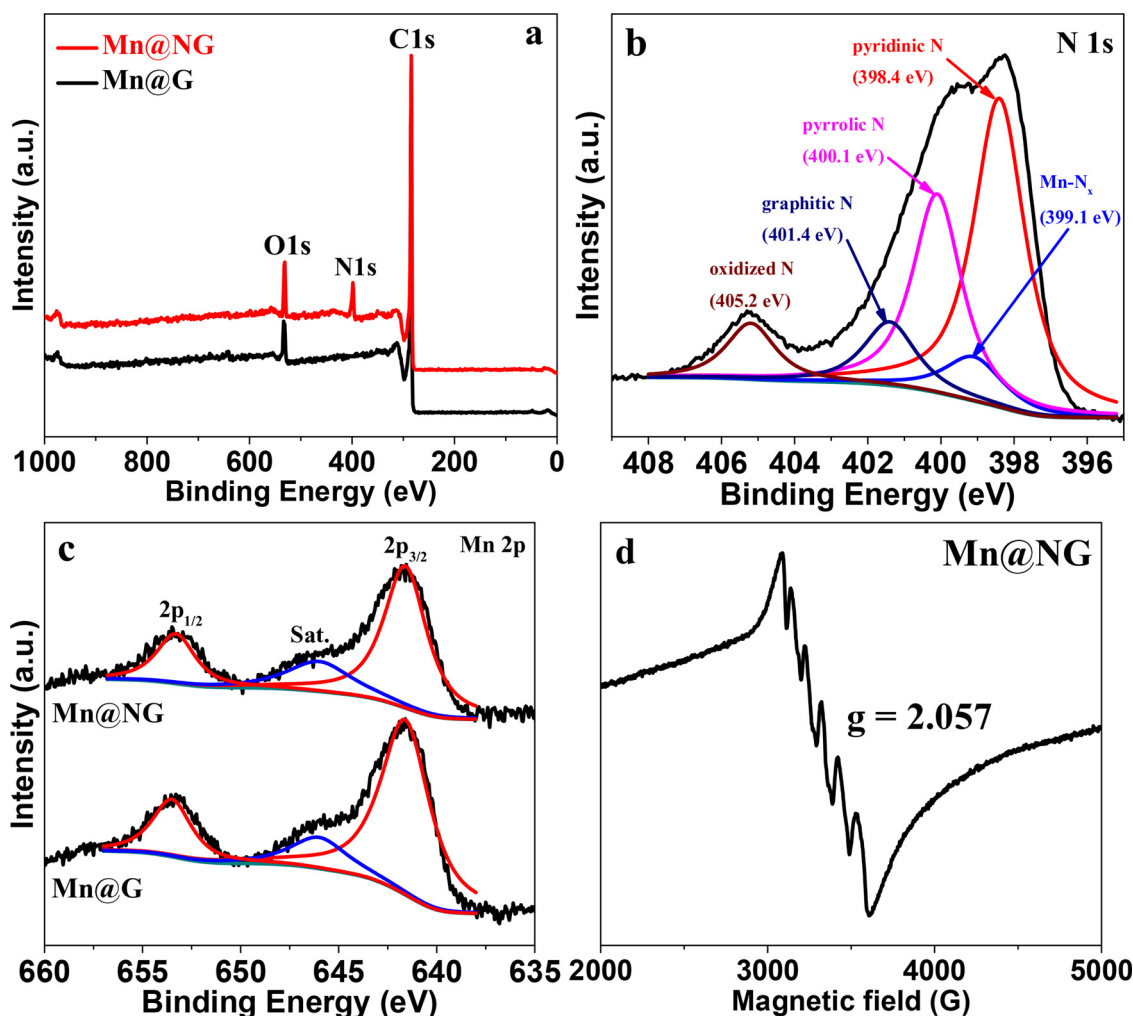


Fig. 2. (a) XPS survey spectra for Mn@G and Mn@NG, (b) high-resolution XPS spectrum of N 1s for Mn@NG, (c) high-resolution XPS spectra of Mn 2p for Mn@G and Mn@NG, (d) EPR spectrum of Mn@NG.

Mn@NG show two obvious signals at 641.6 and 653.4 eV along with a satellite peak at 646.0 eV, indicating the characteristics of Mn^{2+} (Fig. 2c). [30,32] The valence state of Mn in Mn@NG was further analyzed by electron paramagnetic resonance (EPR). The EPR spectrum of Mn@NG displays a $g \approx 2.057$ with six hyperfine lines, indicative of $^{55}\text{Mn}^{2+}$ ($I = 5/2$) in agreement with the XPS results. [33,34]

To precisely investigate the valence state of manganese, X-ray absorption near-edge structure (XANES) was performed. Fig. 3a displays the *ex situ* XANES spectra of Mn foil, MnO, and Mn@NG. The XANES edge profile of Mn@NG is very close to that of MnO but keeps away

from that of Mn foil, demonstrating that the valence state of Mn in Mn@NG is close to 2+ in good agreement with the above XPS and EPR analysis. The extended X-ray absorption fine structure (EXAFS) spectrum of Mn@NG is shown in Fig. 3b. Three shells of light atoms such as O, N, and C are represented by fitting the experimental EXAFS data. The first shell is due to the O_2 adsorbed to Mn center out of the graphene plane. [21,31] The second shell Mn–N is mainly ascribed to the MnN_4C_x structure in the Mn@NG, which is slightly different from the Mn–O in MnO (Fig. 3b). [23,31] No peaks could be detected at around 2.6 Å, which indicates that no Mn–Mn bonds were formed and the manganese

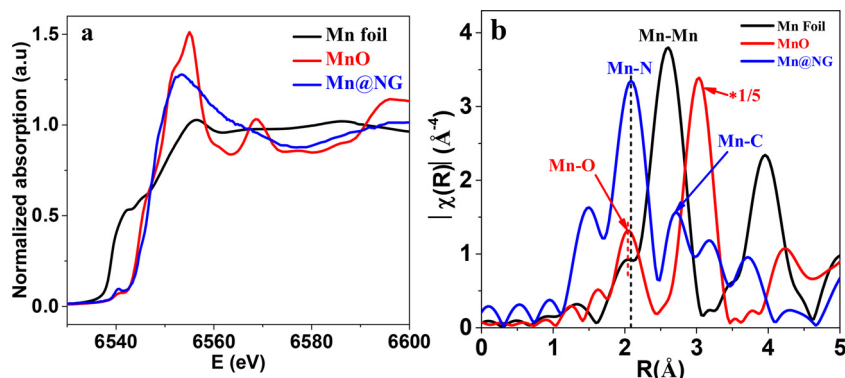


Fig. 3. (a) Normalized XANES spectra at Mn K-edge of Mn foil, MnO, and Mn@NG. (b) FT-EXAFS spectra of Mn foil, MnO, and Mn@NG at the Mn K-edge.

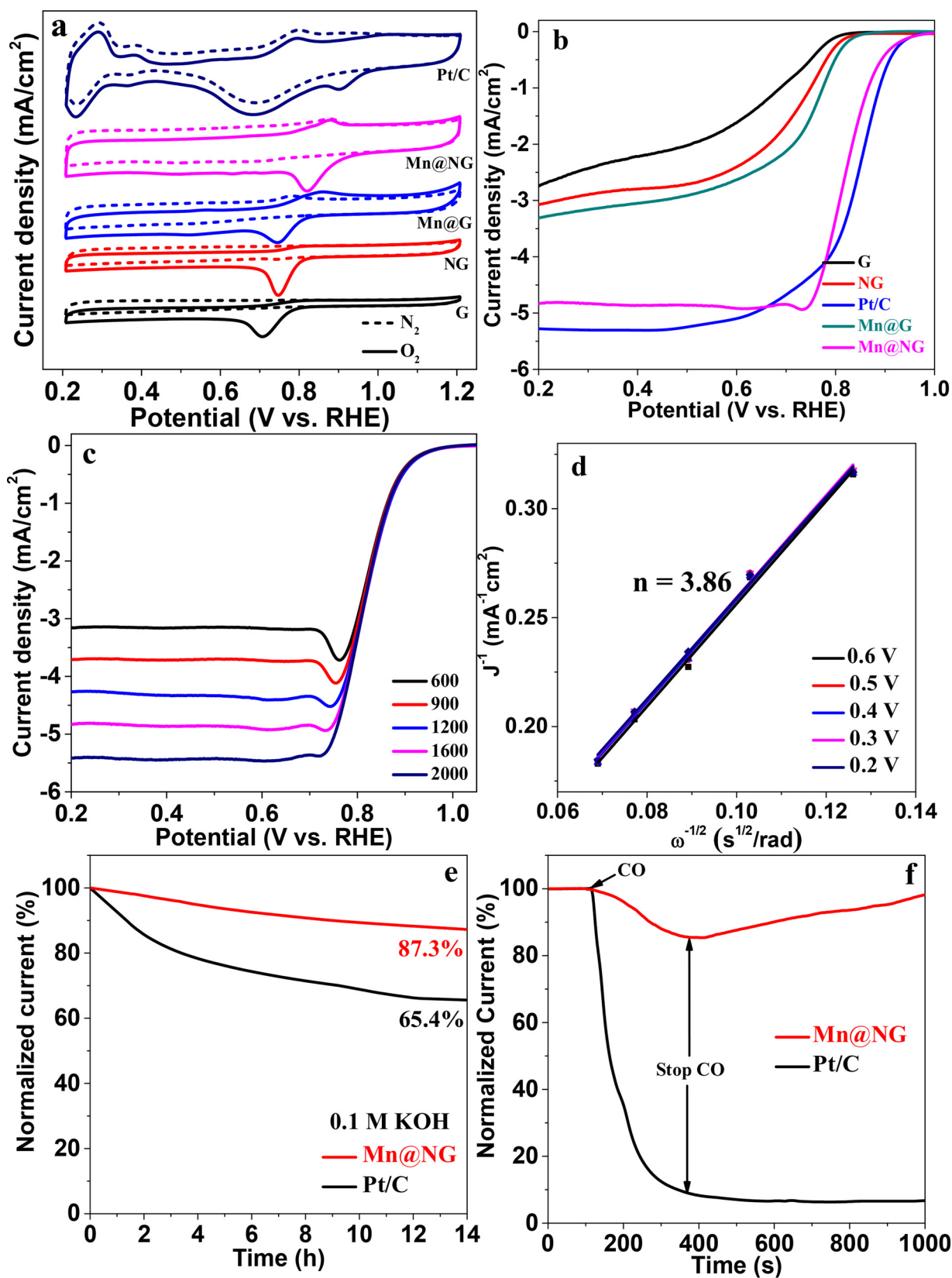


Fig. 4. (a) CV curves of various catalysts in O_2/N_2 -saturated 0.1 M KOH. (b) Polarization curves of Pt/C, G, NG, Mn@G, and Mn@NG (5 $mV \cdot s^{-1}$, 1600 rpm). (c) Polarization curves of Mn@NG at various rotation speeds. (d) K-L plots of the Mn@NG. (e) Chronoamperometric responses (percentage of current retained versus operation time) of Pt/C and Mn@NG kept at 0.70 V vs. RHE in O_2 -saturated 0.1 M KOH electrolyte. (f) Tolerance to carbon monoxide (flow rate: 10 $mL \cdot s^{-1}$) of Mn@NG compared with Pt/C in O_2 -saturated 0.1 M KOH at 0.6 V vs. RHE.

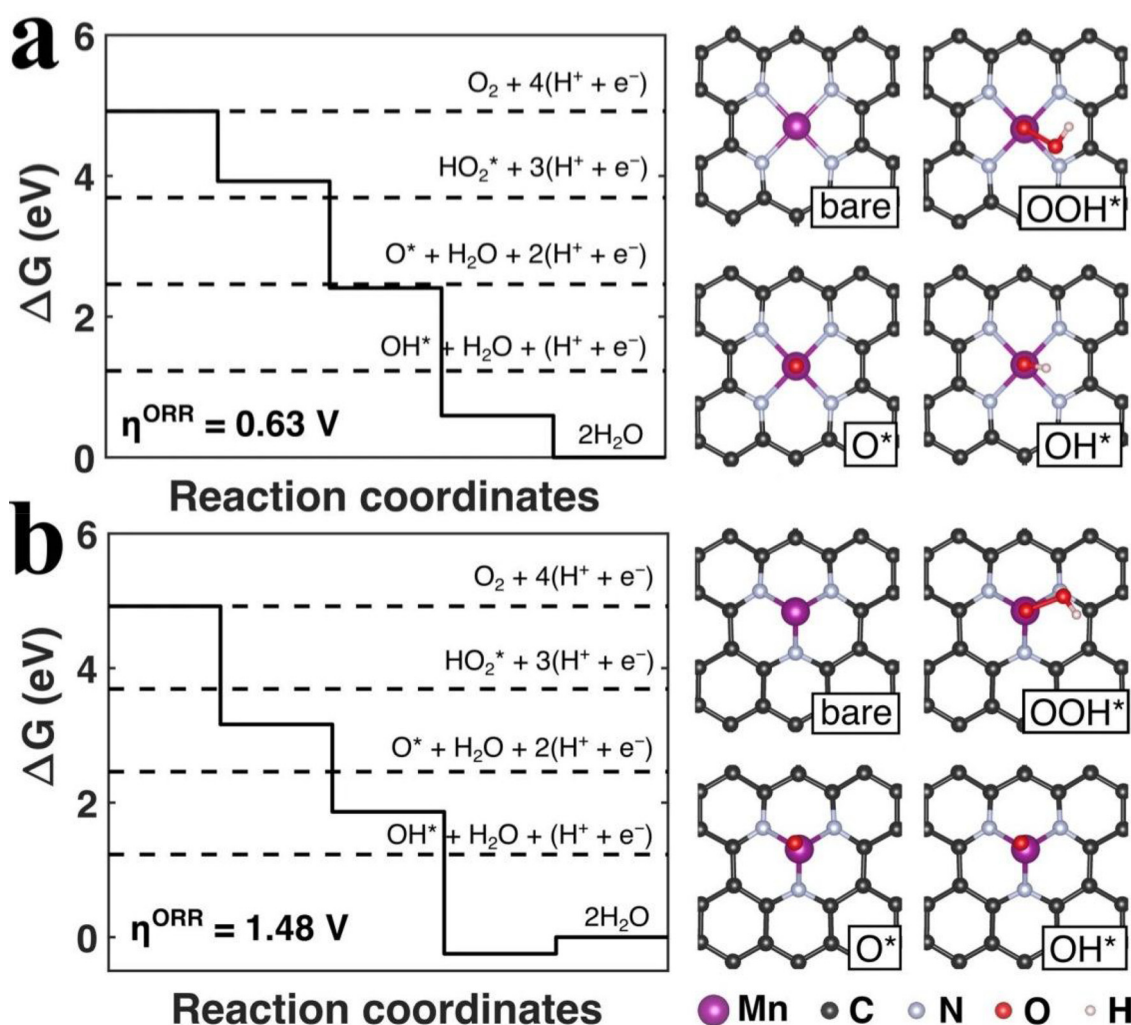


Fig. 5. Free energy diagram for ORR on MnN₄-G (a), and MnN₃-G (b).

ions in Mn@NG are atomically dispersed.

The ORR performance of the graphene (G), nitrogen-doped graphene (NG), Pt/C, Mn@G, and Mn@NG samples prepared are evaluated by cyclic voltammetry (CV) measurements in O₂/N₂-saturated 0.1 M KOH. As shown in Fig. 4a, in comparison to those in N₂-saturated electrolyte, an obviously enhanced cathodic peak for all samples is seen in O₂-saturated one, implying efficient ORR activity. Remarkably, the peak position for Mn@NG is more positive than G, NG, and Mn@G, indicating the best electrocatalytic ORR activity among these samples. LSV measurements are further performed to evaluate the ORR activity of these electrocatalysts (Fig. 4b). The onset potential for G, NG, Mn@G, and Mn@NG is 0.79, 0.82, 0.84, and 0.95 V vs RHE, respectively. Additionally, the half-wave potential ($E_{1/2}$) for G, NG, Pt/C, Mn@G, and Mn@NG is 0.67, 0.71, 0.84, 0.74, and 0.82 V vs RHE, respectively. Notably, Mn@NG exhibits comparable ORR activity with commercial Pt/C (20 wt%) in terms of onset potential, $E_{1/2}$, and diffusion-limiting current density (Fig. 4b).

The effect of annealing temperature on the ORR activity of Mn@NG was measured by CVs and rotating disk electrode (RDE) measurements. As depicted in Fig. S4, when the annealing temperature increases, the resultant intrinsic current density in the ORR exhibits an increase firstly till the annealing temperature reaches 750 °C, and then starts to decrease. Thereby, all the G, NG, Mn@G, and Mn@NG samples are prepared at 750 °C. The annealing temperature might influence the N-doping concentration (Table S1) and the formation of Mn-N₄ active site as discussed below, which could be easily formed at a certain

temperature (e.g. 750 °C). Moreover, the effect of Mn content on the ORR performance was also studied. As exhibited in Fig. S5, the ORR activity increases initially with the Mn content and reaches a peak value for initial Mn content of ca. 0.5 wt.%, beyond which the ORR activity starts to decrease. The excessive Mn would form Mn-containing particles or clusters, which is not conducive to the formation of mononuclear Mn-N-C site. Moreover, the influence of annealing time on ORR activity was also studied. As shown in Fig. S6, the Mn@NG sample annealing for 2 h shows better ORR activity than those annealing for 1, 1.5, 2.5 and 3 h. Taken together, the Mn@NG sample annealed under ammonia at 750 °C for two hours exhibits much high ORR activity in alkaline solution, which is higher or well comparable with previously reported Mn-based electrocatalysts (Table S2).

The electron-transfer number (n) of ORR over Mn@NG was determined by the RDE measurements. As depicted in Fig. S6, the current of Mn@NG rises with augmenting rotation speed because of the improved mass transport at higher speeds. [26] When the rotation speed is low, a cathodic peak at ca. -0.75 V vs. RHE can be observed, indicating that the ORR on Mn@NG is partly absorption-limiting control. [35] The K-L plots of Mn@NG exhibit nice linearity and near coincidence, indicating the first-order reaction kinetics toward ORR (Fig. 4d). [36] The n is confirmed to be ca. 3.86 within the potential range from 0.2 to 0.6 V, revealing the Mn@NG catalyst follows a dominant 4e⁻ oxygen reduction pathway. [37] The transfer electron numbers of Mn@NG between 0.2 and 0.8 V were further investigated by RRDE. As shown in Fig. S7, the n is between 3.82 and 4.0, demonstrating a dominant 4e⁻

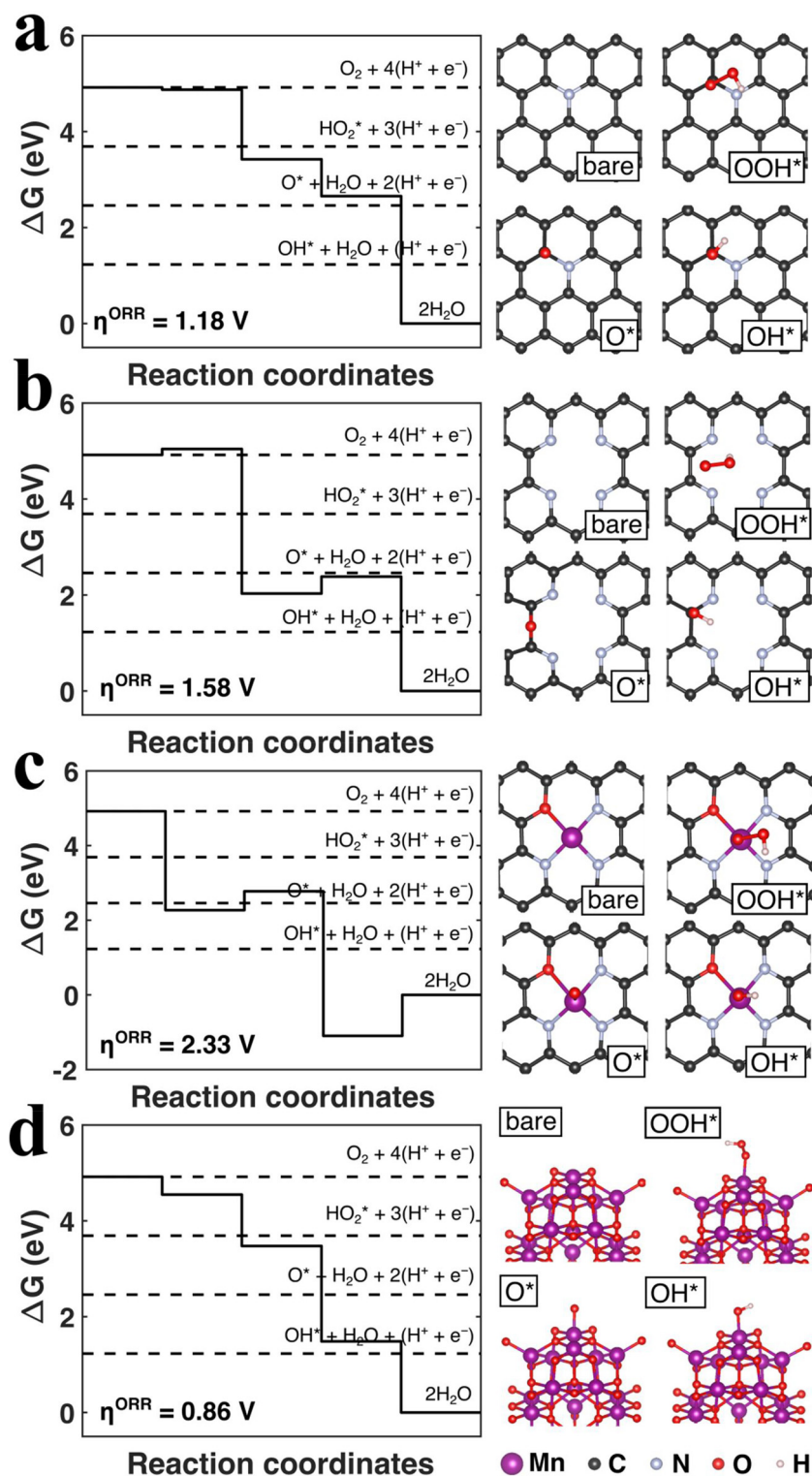


Fig. 6. Free energy diagram for ORR on graphitic-N (a), pyridinic-N (b), $\text{MnN}_3\text{O-G}$ (c), and Mn_3O_4 (001) surface (d).

ORR process. The measured H_2O_2 yields are 2.0 – 10.0%, which hold at a low level. In order to differentiate the direct 4e^- ORR and $2\text{e}^- + 2\text{e}^-$ ORR mechanisms, we investigated the fraction of H_2O_2 produced as a function of catalyst loading. As shown in Figs. S7-S8, when the Mn@NG loadings increase from 0.3 to 1.0 mg cm^{-2} , the H_2O_2 yields maintain in a very low range ($< 10\%$), which further suggests a 4e^- pathway, rather than the $2\text{e}^- + 2\text{e}^-$ pathway. [38] Wu et al. also reported a dominant 4e^- ORR on atomically dispersed manganese

catalysts in acidic media. [23] In addition, we further performed the electrocatalytic performance of Mn@NG for the reduction of hydrogen peroxide. As shown in Fig. S9, the current densities on Mn@NG in O_2 -saturated solutions at 0.4 and 0.7 V are far higher than those observed in N_2 -saturated solutions containing 2 mM H_2O_2 , which affords a direct evidence that Mn@NG is ineffectual for catalysing the reduction of H_2O_2 , further indicating a dominant 4e^- ORR on Mn@NG in alkaline media. [19]

The superior ORR performance of Mn@NG is also demonstrated by its small Tafel slope, which is smaller than that of G, NG, and Mn@G, but slightly higher than that of Pt/C (Fig. S10). The electrochemically active surface area (ECSA) of G, NG, Mn@G, and Mn@NG was measured based on double-layer capacitance. As shown in Fig. S11, the ECSA of Mn@NG is much higher than that of G, NG, and Mn@G, implying the incremental available active sites in Mn@NG.[39] Besides the high ORR activity, Mn@NG also shows good durability. As manifested in Fig. 4e, Mn@NG can maintain ca. 87.3% of the original current density after 14 h of continuous operation, larger than that (65.4%) of Pt/C measured under the same conditions. In addition, Mn@NG displays much better tolerance to carbon monoxide than commercial Pt/C catalysts (Fig. 4f). Moreover, Mn@NG shows stronger tolerance to methanol crossover than Pt/C catalyst. As presented in Fig. S12, very small fluctuations are observed for the Mn@NG electrode after introduction of methanol to the electrolyte, while a dramatic drop in the relative current density is typically observed for Pt/C, implying the tremendous potential of Mn@NG for application in methanol fuel cells.

To acquire insights into the ORR mechanism on Mn@NG, the possible active sites were evaluated by DFT calculations using the well-established computational hydrogen electrode method [40–45]. It is generally accepted that the Mn_4C_x or Mn_3C_x ($\text{M} = \text{Fe}, \text{Co}, \text{Ni}, \text{Mn}$) are the two most probable structures in metal and nitrogen co-doped carbon materials. [23,31,44,45] Therefore, we calculated the theoretical overpotential of ORR on $\text{MnN}_4\text{-G}$ and $\text{MnN}_3\text{-G}$. As shown in Fig. 5, the theoretical overpotential of $\text{MnN}_4\text{-G}$ is 0.63 V, far lower than that of $\text{MnN}_3\text{-G}$ (1.48 V), suggesting that $\text{MnN}_4\text{-G}$ is the primary active site for the observed high ORR activity. In addition, we also calculated the theoretical overpotential of ORR on graphitic-N, pyridinic-N, $\text{Mn}_3\text{O-G}$, and Mn_3O_4 (001) surface as shown in Fig. 6. The theoretical overpotential of metal-free graphitic-N and pyridinic-N sites are predicted to be 1.18 V and 1.58 V, respectively, much higher than that of $\text{MnN}_4\text{-G}$. Additionally, the ORR overpotential on $\text{MnN}_3\text{O-G}$ is as high as 2.33 V due to OH overbinding. This result demonstrates subtle changes in the ligand environment (switching an N with O) of the Mn center would lead to high overpotential, which further justifies the feasibility of the $\text{MnN}_4\text{-G}$ center for catalysing ORR. Finally, the reactivity of $\text{MnN}_4\text{-G}$ system is compared to the Mn_3O_4 (001) surface, which represents for the bulky manganese oxide surface. The overpotential of ORR on Mn_3O_4 (001) is 0.86 V, also higher than that of $\text{MnN}_4\text{-G}$. The high overpotential of Mn_3O_4 (001) is ascribed to the insufficient stabilization of OOH^* , which makes the reduction of O_2 to OOH^* difficult. These results strongly support that the mononuclear Mn site coordinated with four N atoms in the graphene framework should be the ORR active sites of Mn@NG.

3. Conclusions

In conclusion, we developed a convenient strategy for fabricating atomically dispersed manganese electrocatalysts, which can efficiently catalyze ORR with superior activity, excellent durability and strong tolerance to methanol crossover. The mononuclear manganese sites were confirmed by a combination of HAADF-STEM, XAFS and theoretical simulations. Theoretical calculations demonstrate that $\text{MnN}_4\text{-G}$ site should be the main active site for ORR, on which the theoretical overpotential is much lower than that on graphitic-N, pyridinic-N, $\text{MnN}_3\text{-G}$, $\text{MnN}_3\text{O-G}$, and Mn_3O_4 (001) surface. The facile synthetic method to fabricate mononuclear MnN_4C_x sites described here can be further generalized to prepare many other kinds of metal and nitrogen co-doping materials for wide applications including energy storage and conversion, heterogeneous catalysis, and electrocatalysis.

Conflict of interest

None.

Acknowledgments

This work was supported by the Natural Science Foundation of Jilin Province (20180101291JC).

Appendix A. Supplementary data

Supplementary material related to this article can be found, in the online version, at doi:<https://doi.org/10.1016/j.apcatb.2019.117930>.

References

- [1] M. Lefevre, E. Proietti, F. Jaouen, J.-P. Dodelet, *Science* 324 (2009) 71–74.
- [2] G. Wu, K.L. More, C.M. Johnston, P. Zelenay, *Science* 332 (2011) 443–447.
- [3] A.A. Gewirth, J.A. Varnell, A.M. DiAscro, *Chem. Rev.* 118 (2018) 2313–2339.
- [4] H.T. Chung, D.A. Cullen, D. Higgins, B.T. Sneed, E.F. Holby, K.L. More, P. Zelenay, *Science* 357 (2017) 479–483.
- [5] Z. Chen, D. Higgins, A. Yu, L. Zhang, J. Zhang, *Energy Environ. Sci.* 4 (2011) 3167–3192.
- [6] R. Lin, X. Cai, H. Zeng, Z. Yu, *Adv. Mater.* 30 (2018) 1705332.
- [7] Y. Chen, S. Ji, C. Chen, Q. Peng, D. Wang, Y. Li, *Joule* 2 (2018) 1242–1264.
- [8] C. Hu, L. Dai, *Angew. Chem., Int. Ed.* 55 (2016) 11736–11758.
- [9] H. Bin Wu, X.W. Lou, *Sci. Adv.* 3 (2017) eaap9252.
- [10] Z. Lu, G. Chen, S. Siahrostami, Z. Chen, K. Liu, J. Xie, L. Liao, T. Wu, D. Lin, Y. Liu, T.F. Jaramillo, J.K. Norskov, Y. Cui, *Nat. Catal.* 1 (2018) 156–162.
- [11] D. Guo, R. Shibuya, C. Akiba, S. Saji, T. Kondo, J. Nakamura, *Science* 351 (2016) 361–365.
- [12] K. Gong, F. Du, Z. Xia, M. Durstock, L. Dai, *Science* 323 (2009) 760–764.
- [13] S. Liu, K. Mase, C. Bougher, S.D. Hicks, M.M. Abu-Omar, S. Fukuzumi, *Inorg. Chem.* 53 (2014) 7780–7788.
- [14] J. Jung, S. Liu, K. Ohkubo, M.M. Abu-Omar, S. Fukuzumi, *Inorg. Chem.* 54 (2015) 4285–4291.
- [15] Z. Ou, A. Lü, D. Meng, S. Huang, Y. Fang, G. Lu, K.M. Kadish, *Inorg. Chem.* 51 (2012) 8890–8896.
- [16] T. Yamaguchi, K. Tsukamoto, O. Ikeda, R. Tanaka, T. Kuwabara, K. Takahashi, *Electrochim. Acta* 55 (2010) 6042–6048.
- [17] F. Isaacs, W. Dehaen, W. Maes, T.H. Ngo, D. Ruiz-León, F. Herrera, R. Arce, M.C. Arévalo, M.J. Aguirre, *Int. J. Electrochem. Sci.* 8 (2013) 3406–3418.
- [18] W. Zhang, W. Lai, R. Cao, *Chem. Rev.* 117 (2017) 3717–3797.
- [19] J. Meng, H. Lei, X. Li, J. Qi, W. Zhang, R. Cao, *ACS Catal.* 9 (2019) 4551–4560.
- [20] H. Zhang, J. Nai, L. Yu, X.W. Lou, *Joule* 1 (2017) 77–107.
- [21] A. Zitolo, V. Goellner, V. Armel, M.-T. Sougrati, T. Mineva, L. Stievano, E. Fonda, F. Jaouen, *Nat. Mater.* 14 (2015) 937–942.
- [22] P. Yin, T. Yao, Y. Wu, L. Zheng, Y. Lin, W. Liu, H. Ju, J. Zhu, X. Hong, Z. Deng, G. Zhou, S. Wei, Y. Li, *Angew. Chem., Int. Ed.* 55 (2016) 10800–10805.
- [23] J. Li, M. Chen, D.A. Cullen, S. Hwang, M. Wang, B. Li, K. Liu, S. Karakalos, M. Lucero, H. Zhang, *Nat. Catal.* 1 (2018) 935–945.
- [24] Y. Zhong, X. Liang, Z. He, W. Tan, J. Zhu, P. Yuan, R. Zhu, H. He, *Appl. Catal. B: Environ.* 150 (2014) 612–618.
- [25] J. Suntivich, H.A. Gasteiger, N. Yabuuchi, H. Nakanishi, J.B. Goodenough, Y. Shao-Horn, *Nat. Chem.* 3 (2011) 546–550.
- [26] T. Li, B. Xue, B. Wang, G. Guo, D. Han, Y. Yan, A. Dong, *J. Am. Chem. Soc.* 139 (2017) 12133–12136.
- [27] K. Lei, X. Han, Y. Hu, X. Liu, L. Cong, F. Cheng, J. Chen, *Chem. Commun. (Camb.)* 51 (2015) 11599–11602.
- [28] Z. Lu, G. Xu, C. He, T. Wang, L. Yang, Z. Yang, D. Ma, *Carbon* 84 (2015) 500–508.
- [29] Y. Ni, Z. Chen, F. Kong, Y. Qiao, A. Kong, Y. Shan, *Electrochim. Acta* 272 (2018) 233–241.
- [30] Y. Wang, X. Ding, F. Wang, J. Li, S. Song, H. Zhang, *Chem. Sci.* 7 (2016) 4284–4290.
- [31] J. Guan, Z. Duan, F. Zhang, S.D. Kelly, R. Si, M. Dupuis, Q. Huang, J.Q. Chen, C. Tang, C. Li, *Nat. Catal.* 1 (2018) 870–877.
- [32] Y. Sun, X. Hu, W. Luo, F. Xia, Y. Huang, *Adv. Funct. Mater.* 23 (2013) 2436–2444.
- [33] S. Nandi, K. Das, A. Datta, D. Banerjee, S. Roy, T.K. Mondal, D. Mandal, P.K. Nanda, T. Akitsu, S. Tanaka, C. Sinha, *J. Mol. Struct.* 1133 (2017) 574–579.
- [34] M. He, X. Li, Y. Liu, J. Li, *Inorg. Chem.* 55 (2016) 5871–5879.
- [35] Z.-F. Ma, X.-Y. Xie, X.-X. Ma, D.-Y. Zhang, Q. Ren, N. Heß-Mohr, V.M. Schmidt, *Electrochem. commun.* 8 (2006) 389–394.
- [36] I.M. Mosa, S. Biswas, A.M. El-Sawy, V. Botu, C. Guild, W. Song, R. Ramprasad, J.F. Rusling, S.L. Suib, *J. Mater. Chem. A Mater. Energy Sustain.* 4 (2016) 620–631.
- [37] Y. Liang, Y. Li, H. Wang, J. Zhou, J. Wang, T. Regier, H. Dai, *Nat. Mater.* 10 (2011) 780–786.
- [38] A. Bonakdarpour, M. Lefevre, R. Yang, F. Jaouen, T. Dahn, J.-P. Dodelet, J.R. Dahn, *Electrochem. Solid-State Lett.* 11 (2008) B105–B108.
- [39] C.C. McCrory, S. Jung, J.C. Peters, T.F. Jaramillo, *J. Am. Chem. Soc.* 135 (2013) 16977–16987.
- [40] J.K. Norskov, J. Rossmeisl, A. Logadottir, L. Lindqvist, J.R. Kitchin, T. Bligaard, H. Jonsson, *J. Phys. Chem. B* 108 (2004) 17886–17892.
- [41] I.C. Man, H.-Y. Su, F. Calle-Vallejo, H.A. Hansen, J.I. Martinez, N.G. Inoglu, J. Kitchin, T.F. Jaramillo, J.K. Norskov, J. Rossmeisl, *ChemCatChem* 3 (2011) 1159–1165.
- [42] M. Garcia-Mota, M. Bajdich, V. Viswanathan, A. Vojvodic, A.T. Bell, J.K. Norskov, *J. Phys. Chem. C* 116 (2012) 21077–21082.
- [43] H.-Y. Su, Y. Gorlin, I.C. Man, F. Calle-Vallejo, J.K. Norskov, T.F. Jaramillo, J. Rossmeisl, *Phys. Chem. Chem. Phys.* 14 (2012) 14010–14022.
- [44] H. Xu, D. Cheng, D. Cao, X.C. Zeng, *Nat. Catal.* 1 (2018) 339–348.
- [45] H. Fei, J. Dong, Y. Feng, C.S. Allen, C. Wan, B. Voloskiy, M. Li, Z. Zhao, Y. Wang, H. Sun, *Nat. Catal.* 1 (2018) 63–72.